Test of a Method to Calculate Near-Bank Velocity and Boundary Shear Stress

Jason W. Kean, A.M.ASCE[1]; Roger A. Kuhnle, M.ASCE[2]; J. Dungan Smith, A.M.ASCE[3]; Carlos V. Alonso, M.ASCE[4]; and Eddy J. Langendoen, M.ASCE[5]

Abstract: Detailed knowledge of the flow and boundary shear stress fields near the banks of natural channels is essential for making accurate calculations of rates of near-bank sediment transport and geomorphic adjustment. This paper presents a high-resolution laboratory data set of velocity and boundary shear stress measurements and uses it to test a relatively simple, fully predictive, numerical method for determining these distributions across the cross-section of a straight channel. The measurements are made in a flume with a fairly complex cross-section that includes a simulated, cobble-roughened floodplain. The method tested is that reported by Kean and Smith in Riparian Vegetation and Fluvial Geomorphology in 2004, which is modified here to include the effects of drag on clasts located in the channel. The calculated patterns of velocity and boundary shear stress are shown to be in reasonable agreement with the measurements. The principal differences between the measured and calculated fields are the result of secondary circulations, which are not included in the calculation. Better agreement with the structure of the measured streamwise velocity field is obtained by distorting the calculated flow field with the measured secondary flow. Calculations for a variety of narrower and wider configurations of the original flume geometry are used to show how the width-to-depth ratio affects the distribution of velocity and boundary shear stress across the channel.

DOI: 10.1061/(ASCE)HY.1943-7900.0000049

CE Database subject headings: Shear stress; Hydraulic roughness; Sediment transport; River bank erosion; Drag.

Introduction

Accurate determination of the distribution of boundary shear stress on and near the banks of natural channels is essential for addressing a variety of problems in fluvial geomorphology and stream restoration. These problems include (1) calculation of rates of lateral erosion in rivers; (2) determination of sediment transport in rills and gullies; and (3) calculation of accurate stage-discharge relations in narrow streams. Determination of the near-bank boundary shear stress in natural channels requires (1) the ability to quantify the roughness and form drag of irregular banks; and (2) a means to determine how both the bank geometry and the relative roughness of the bed and the bank affect the distribution of stress. Recently, a series of methods have been developed with the goal of addressing these important aspects of the problem. The form drag and hydrodynamic resistance of small-scale topographic features commonly found on the banks of natural channels can be calculated using the approaches of Kean and Smith (2006a,b). Drag on the stems and branches of rigid vegetation, which is another roughness element commonly found on banks of natural channels, can be determined using the method of Kean and Smith (2004). The Kean and Smith method determines the distribution of streamwise boundary shear stress across the entire wetted-perimeter of the channel cross section, and testing this feature of their model is the primary focus of this paper.

Much work concerning the distribution of near-bank boundary shear stress in channels has been conducted in laboratory flumes with prismatic cross sections. A basic understanding of how the perimeter-averaged stress is partitioned between the bed and the walls of rectangular channels has come from classic flume sediment transport studies, which required methods to account for the effects of sidewall friction on the rates of sediment transport (e.g., Einstein 1942; Vanoni and Brooks 1957; Williams 1970; Cheng and Chua 2005). Other studies have made detailed measurements of velocity and boundary shear stress in straight laboratory flumes to study the complex patterns of boundary shear stress distribution across the channel (e.g., Knight et al. 1984; Tominaga and Nezu 1991; Knight et al. 1994). Such measurements have been used subsequently to validate three-dimensional numerical flow and turbulence models (e.g., Naot et al. 1993). These nonsediment transport related investigations have placed particular emphasis on resolving secondary circulations in the flume and determining their effects on the distribution of boundary shear stress. Some of the secondary circulations documented by these studies are generated by the distinct corners of the flume boundaries (e.g., the corner between the flume wall and the bed) (see Liggett 1994). These types of circulations (classified as Prandtl's second kind of secondary circulation) are produced by turbulent anisotropy of the cross-stream and vertical velocity fluctuations (Nezu and Nakagawa 1993). In natural channels, which do not have such corners,

[1]Research Hydrologist, U.S. Geological Survey, Denver, CO 80225–0046 (corresponding author). E-mail: jwkean@usgs.gov

[2]Research Hydraulic Engineer, National Sedimentation Laboratory, USDA-Agricultural Research Service, Oxford, MS 38655-1157.

[3]Research Hydrologist, U.S. Geological Survey, Boulder, CO 80303.

[4]Supervisory Research Hydraulic Engineer, National Sedimentation Laboratory, USDA-Agricultural Research Service, Oxford, MS 38655-1157.

[5]Research Hydraulic Engineer, National Sedimentation Laboratory, USDA-Agricultural Research Service, Oxford, MS 38655-1157.

Note. This manuscript was submitted on June 1, 2007; approved on January 11, 2009; published online on February 6, 2009. Discussion period open until December 1, 2009; separate discussions must be submitted for individual papers. This paper is part of the ***Journal of Hydraulic Engineering***, Vol. 135, No. 7, July 1, 2009. ©ASCE, ISSN 0733-9429/2009/7-588–601/$25.00.

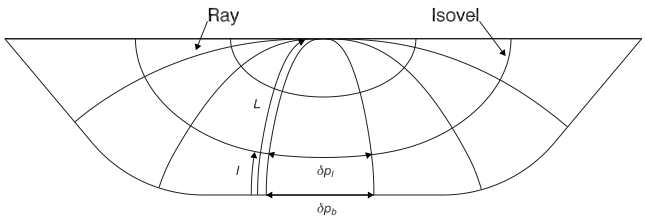

Fig. 1. Example cross section showing ray-isovel orthogonal coordinate system

other more dominant types of secondary circulations associated with channel irregularity are usually present and have a substantial effect on the distribution of boundary shear stress. One of the most common of these latter types of secondary circulations is produced by channel curvature (Prandtl's first kind of secondary circulation).

Early work regarding the determination of near-bank boundary shear stress in natural channels focused on straight channels with gradually sloping banks. Lundgren and Jonsson (1964) and later Parker (1978) developed analytic solutions for the streamwise distributions of stress across the channel, which included the effects of the bank on the stress. Although simple analytic methods are available to determine the distribution of stress in prismatic channels with steep banks (e.g., Yang and Lim 2005), the calculation of boundary shear stress distributions in channels of arbitrary cross-sectional geometry currently requires the use of numerical methods. One approach, which is beginning to be used more extensively, is to apply fully three-dimensional computational fluid dynamical (CFD) algorithms to resolve near-bank patterns of boundary shear stress. A current drawback to this approach is that it is computationally very intensive, which limits the domain that can be modeled. This limitation, however, will become less of an issue as available computing power continues to increase.

An alternative to the above-mentioned methods for determining near-bank boundary shear stress is to distribute stress along lines (rays) that are perpendicular to lines of constant velocity (isovels) as shown in Fig. 1. Leighly (1932) first used the ray-isovel approach empirically to determine the stress distribution in natural channels from measured velocity fields. The theoretical work of Houjou et al. (1990) developed a turbulence closure based on the ray-isovel concept and applied it in the form of a numerical model to determine the distributions of velocity and shear stress in straight, rectangular channels with known bed and bank roughnesses. An alternative approach for calculating isovels in channels based on an analogy with electromagnetic theory has been developed by Maghrebi and Ball (2006). Unlike the completely predictive model of Houjou et al. (1990), this latter approach requires a single measurement of velocity to scale the calculated velocity field. The Houjou et al. (1990) model was generalized recently by Kean and Smith (2004) to accommodate channels of arbitrary cross section and to include the effects of drag on rigid bank vegetation. Although, flow models employing the ray-isovel turbulence closure do not determine secondary circulations, they require substantially less computational effort than fully three-dimensional flow models, and they can more easily accommodate downstream and cross-stream variations of physical and biological roughness elements. Moreover, in order to calculate "secondary circulations" in a general flow problem the primary flow and its associated turbulence field must be accurately resolved. Despite the relative simplicity of the ray-isovel framework compared to CFD approaches, the ray-isovel approach can be used for determining distributions of velocity and boundary shear stress in complex natural channels (see Griffin et al. 2005; Kean and Smith 2005), and it provides a foundation for "secondary circulation" calculations.

The purpose of this paper is to (1) make a comprehensive laboratory data set collected by three of the authors available to the research community for making detailed tests of predictive flow models and (2) perform a specific test of the ray-isovel approach employed by Kean and Smith (2004). The measurements were made in a straight flume with a simulated, cobble-roughened floodplain. A minor extension to the method of Kean and Smith (2004) is made here to determine the form drag on the floodplain cobbles and their effects on the velocity and boundary shear stress. The high resolution of the measurements and the relatively complex shape and roughness characteristics of the flume provide data for a rigorous test of a flow model, such as Kean and Smith (2004). Owing to the predictive nature of the model and the comprehensive nature of the data set, the discrepancies are identified and their likely causes are examined. The model is then applied to examine the patterns of boundary shear stress in hypothetical narrower and wider channels having similar geometric and roughness characteristics as the study flume.

Ray–Isovel Model

The momentum equation for steady, streamwise uniform flow in a channel with lateral boundaries is

$$0 = \rho g \sin(\theta) + \frac{\partial \tau_{yx}}{\partial y} + \frac{\partial \tau_{zx}}{\partial z} \tag{1}$$

where ρ=fluid density; g=acceleration of gravity; and θ=angle deviation of the water surface from horizontal. The stress terms τ_{zx} and τ_{yx} are the zx and yx components of the deviatoric stress tensor [see Kundu (1990)], where x, y, and z are the downstream, cross-stream, and vertical directions, respectively. Despite the lack of a general analytic solution, the distribution of fluid stress throughout a channel of arbitrary cross section can be defined in an intuitive manner using the natural, curvilinear coordinate system of the flow. This coordinate system consists of rays that are perpendicular to isovels as shown in Fig. 1. The rays, which are perpendicular to the boundary and extend to the water surface, define streamwise surfaces of zero cross-ray shear. Consequently, the downstream component of the weight of water between two adjacent rays is balanced completely by friction on the length of wetted perimeter that separates the rays at the boundary. The boundary shear stress defined by that force balance is given by

$$\tau_b = \rho g \sin(\theta) \frac{\int_0^L p(l_d) dl_d}{p_b} \tag{2}$$

where l represents the distance along a ray from the boundary (l_d=dummy integration variable along the path of a ray), $p(l_d)$ =length along an isovel between two rays, and p_b=perimeter length along the boundary between two rays. Note that $p(0)=p_b$. The integral in the numerator represents the total area between two rays. The limits of integration follow the length of a ray from the boundary ($l=0$) to the surface ($l=L$). This formulation can be originally attributed to Leighly (1932), and it is analogous to the expression for the average boundary shear stress in a channel given by $\bar{\tau}_b=\rho g \sin(\theta) A/P$, where A is the total area of the cross section and P is the full-wetted perimeter. The shear stress along

Fig. 2. View looking up the USDA-NSL 100 ft flume. The acoustic Doppler current velocimeter is shown on the right side of picture. The width of the flume including the floodplain is 1.22 m.

each ray in the interior of the channel, τ_{lx}, is given by a similar expression to (2), which is

$$\tau_{lx} = \rho g \sin(\theta) \frac{\int_l^L p(l_d) dl_d}{p(l)} \tag{3}$$

The ray-isovel coordinate system also is used to define a scalar eddy viscosity that relates τ_{lx} to the mean velocity gradient along a ray through the expression $\tau_{lx} = \rho K(\partial u / \partial l)$. The functional form of K near the boundary used by Kean and Smith (2004) is

$$K = \kappa u_* l \left(\frac{\tau_{lx}}{\tau_b} \right) \tag{4}$$

where κ is von Karman's constant, which equals 0.408 (Long et al. 1993); and u_* is the shear velocity, which equals $\sqrt{\tau_b / \rho}$. In their formulation, the eddy viscosity increases along each ray according to (4) until it reaches the channel scale eddy viscosity, K_o. For the channel of concern in this paper, the appropriate length scale for K_o is the maximum flow depth, H. This gives $K_o = \kappa [g \sin(\theta) R]^{1/2} H / \beta$, where β is a constant equal to 6.24 and R is the hydraulic radius, $R = A/P$. The constant 6.24 is the value of β shown by Shimizu (1989) to give the best agreement with the laboratory-measured velocity profile of Einstein and Chien (1955).

By defining the spatial variation of the eddy viscosity for an entire streamwise uniform channel, Eq. (1) can be rewritten as

$$0 = \rho g \sin(\theta) + \frac{\partial}{\partial y} \left(\rho K \frac{\partial u}{\partial y} \right) + \frac{\partial}{\partial z} \left(\rho K \frac{\partial u}{\partial z} \right) \tag{5}$$

The boundary conditions for Eq. (5) are that $\partial u / \partial z = 0$ at the water surface and $u = 0$ at the roughness length $l = l_o$. For homogenous surfaces, such as the boundaries of the study flume, l_o can be specified as a function of u_* and the equivalent grain size diameter of the surface, k_s, based on the experimental work of Nikuradse (1933). Different techniques are required to estimate l_o for the hydraulically rough flow conditions present near irregular surfaces characteristic of natural channels [see Kean and Smith (2005, 2006a,b) for a discussion of determining l_o for natural bed and bank surfaces].

Form Drag on Roughness Elements

Kean and Smith (2004) extended the ray-isovel model framework of Houjou et al. (1990) to include the effects of form drag due to roughness elements. This was accomplished by incorporating the drag force per unit volume on the roughness elements directly into the momentum equation. The roughness elements in that study were rigid stems and branches of woody vegetation and were modeled as circular cylinders. In this paper, the roughness elements are similar-sized cobbles fixed to the boundary of the laboratory flume in a regular staggered array (see Figs. 2 and 3). The effects of the cobbles on the velocity and boundary shear stress fields can be determined using an approach similar to the one taken by Kean and Smith (2004) for rigid vegetation. The drag force per unit volume on the cobbles is given by

$$F = \frac{1}{2} \rho C_D \frac{d}{\lambda^2} u_{\text{ref}}^2 \tag{6}$$

where C_D = drag coefficient of a single cobble; u_{ref} = reference velocity; λ = mean distance between cobbles; and d = local width of the cobbles at an elevation z. The ratio d/λ^2 represents the local cross-sectional area of the cobbles oriented perpendicular to the flow direction $(d \cdot dz)$ divided by the volume that slice affects $(\lambda^2 \cdot dz)$. This ratio can vary as a function of y and z to accommodate changes in cobble size and spatial density. In this application, the cobbles are modeled as identical spheres of diameter D. For the situation where the spheres rest on a surface of elevation $z = 0$, the variation of the local cobble width with z is given by $d = \sqrt{D^2 - (2z - D)^2}$. The basic approach used here to model the natural floodplain cobbles can be generalized to accommodate a size distribution of particles and/or other particle geometries, such as ellipsoids.

The square of the reference velocity for determining drag on

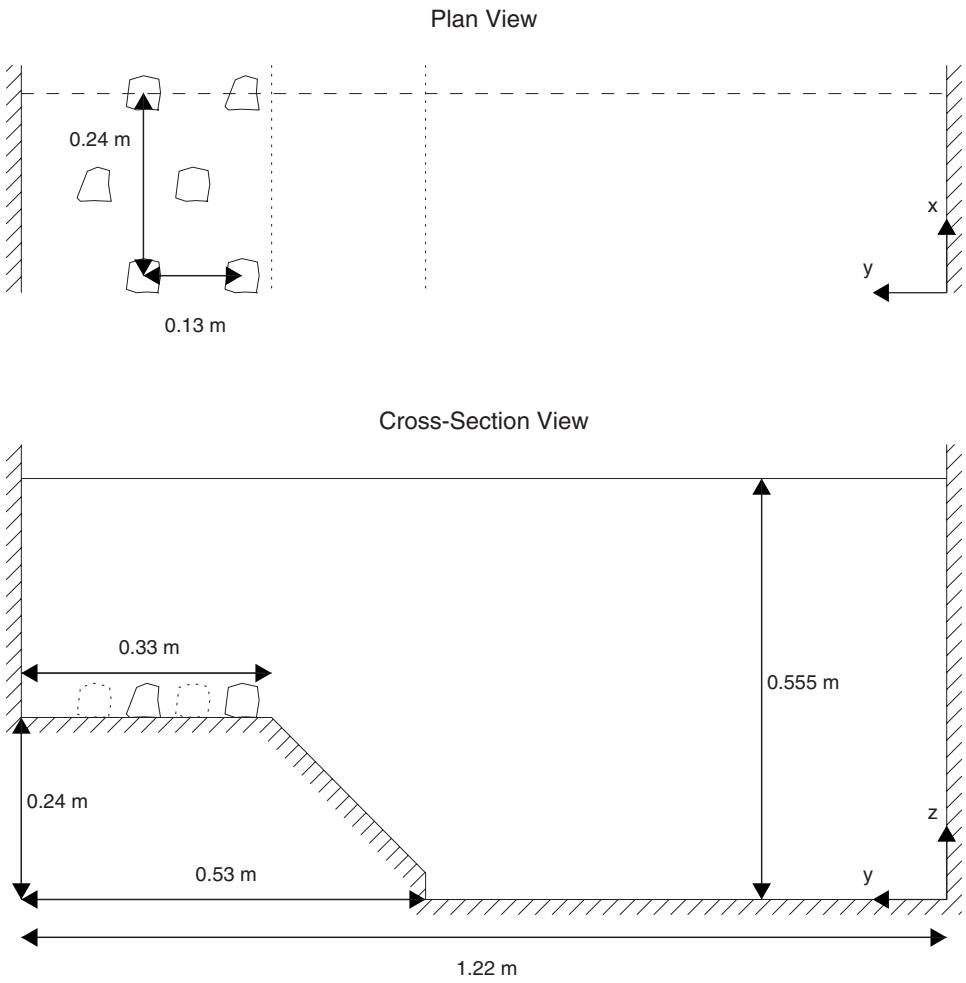

Fig. 3. Flume dimensions. The mean diameter of the cobbles is 4.5 cm. The bank slope is 45°. Cross-sectional view is looking downstream. The dashed line in the plan view denotes the cross section, where velocity measurements were taken.

an individual cobble is defined to be the average squared velocity that would be present if the cobble were removed from the flow, with the average taken over the volume the object occupied. Defining u_{ref} in this manner allows us to use C_D for an individual cobble. The Reynolds numbers of the experiment are in the turbulent range where C_D for a sphere is nearly constant and equal to about 0.45 (Wiberg and Smith 1991). If, as is the case in this study, the drag force is expressed on a per volume basis rather than for an entire cobble, then the same value of C_D should be used, but u_{ref} can be approximated by the local mean velocity $u(y,z)$. Including the drag per unit volume in the momentum balance gives

$$0 = \rho g \sin(\theta) + \frac{\partial}{\partial y}\left(\rho K \frac{\partial u}{\partial y}\right) + \frac{\partial}{\partial z}\left(\rho K \frac{\partial u}{\partial z}\right) - \frac{1}{2}\rho C_D \frac{d}{\lambda^2} u^2 \quad (7)$$

In addition to reducing flow velocities, drag on the cobbles also affects the turbulence and the shear stress. Owing to the fact that the cobbles occupy only a very small fraction of the total cross-sectional area of the study channel, the local effects of the cobbles on the turbulence are not considered in this paper. The appropriate length scale of turbulent mixing within a field of clasts, however, can be estimated using an approach suggested by Wiberg and Smith (1991). The effects of the cobbles on boundary shear stress (τ_b) are determined in this paper by subtracting the total drag force within the area between two adjacent rays from the downstream component of the weight of water in that area. This may be expressed as

$$\tau_b = \frac{\int_0^L [\rho g \sin(\theta) - \bar{F}(l_d)] p(l_d) dl_d}{p_b} \quad (8)$$

where $\bar{F}(l)$ = average drag force per unit volume along the length of an isovel between two adjacent rays.

In summary, the required inputs to the model are geometric parameters: channel cross-sectional geometry (which is arbitrary), flow depth (H), angle deviation of the water surface from horizontal (θ), roughness height of the boundary (l_o), and the diameter (D), and spacing (λ) of the cobbles. These parameters are known from the experimental setup, which will be described in the next section. Solutions for the velocity and boundary shear stress fields can be obtained by numerical solution of Eqs. (2)–(8). Starting with an initial guess of the boundary shear stress distribution and the velocity in the interior, the computation alternatively solves the momentum Eq. (7) for u and Eqs. (8), (3), and (4) for τ_b, τ_{lx}, and K until the flow solution converges. To reduce the number of grid points required in the calculation, the velocity within a short distance of the boundary (0.01 m) is computed using the law of the wall $[u = (u_*/\kappa)\ln(l/l_o)]$. It is important to

Table 1. Summary of Flow Conditions in Experiment

Discharge[a] Q (m^3/s)	Slope[b] S (m/m)	Depth H (m)	Area A (m^2)	k_s walls/bed (mm)	k_s floodplain/slope (mm)	Cobble mean diam. (cm)
0.396	0.00036	0.555	0.57	0.235	0.8	4.5

[a]From flume's Venturi meter.

[b]Based on perimeter average of measured stress, $S=\bar{\tau}_b/(\rho g R)$.

note that in this paper the model is applied without making any empirical adjustments to model parameters (i.e., no model tuning or fitting is conducted).

Laboratory Measurements

Measurements of velocity and boundary shear stress measurements were made in a 30.5 m long, 1.22 m wide flume at the U.S. Department of Agriculture National Sedimentation Laboratory (USDA-NSL). A steady discharge was maintained for the entire time period over which the measurements were collected. A photograph and diagram of the flume geometry is shown in Figs. 2 and 3. The vertical walls and bed of the flume are made of aluminum and the slope and horizontal surface of a simulated floodplain are constructed of sheet metal with a layer of sand (0.8 mm median diameter) glued to the surface. The horizontal surface of the "floodplain" contains a staggered array of similar-sized cobbles having a mean diameter of 4.5 cm and a spacing shown in Fig. 3. A summary of the flow conditions during the measurements is given in Table 1.

Over 1500 measurements of the downstream, cross-stream, and vertical components of velocity were made in a single cross section using an acoustic Doppler velocimeter (ADV). The ADV was rigidly mounted on a precision three-axis computer-controlled positioning system. The ADV was moved to all of the measurement locations by sending commands to the stepper motors, and the mounting was not changed over the course of data collection. Each velocity measurement was averaged for 120 sec at a sampling rate of 50 Hz. The velocity measurements were processed using the public domain software WinADV (Wahl 2000), which filtered the data to reject points with correlation coefficient of <0.70. Repeated measurements ($n=6$) at the same location (0.919 m from left wall viewed downstream, 0.300 m above the bed, and 19.5 m downstream from the flume entrance) yielded standard errors of 0.1, 3.9, and 1.0% of the mean velocity in the streamwise (x), cross-stream (y), and vertical (z) directions, respectively.

The measurement cross section was located 19.5 m downstream of the entrance to the flume. In the interior of the flume, measurements were spaced 3 cm apart in both the y and z directions. Within 2 cm of the flume boundaries, velocity measurements were spaced 0.5 cm apart in the directions normal and parallel to the boundary. No velocity measurements were made within 7.5 cm of the water surface due to the size of the ADV. The cross-stream and vertical velocities in the flume, which are almost two orders of magnitude smaller than the downstream velocity, are particularly sensitive to the angle alignment of the ADV relative to the y- and z-axes. On the basis of the computer-controlled ADV mounting and positioning system that was used, we are confident the ADV alignment was constant for all measurements. In order to account for possible constant alignment error, the orientation of the ADV about the y- and z-axes was adjusted to minimize both the vertical discharge across all horizontal transects of the measurement section and the cross-stream discharge across all vertical transects. This adjustment resulted in $<1°$ of rotation about the y- and z-axes.

Measurements of boundary shear stress were made with a 2.35 mm diam Preston tube (Preston 1954). The approach uses the law of the wall to convert measurements of dynamic pressure obtained using a total head tube to boundary shear stress (e.g., Patel 1965; Hwang and Larsen 1963; Nece and Smith 1970; Head and Rechenberg 1972). Measured pressures were converted to shear stress using the efficient computational procedure of Wu and Rajaratnam (2000), which is based on the pressure-stress calibration of Hollingshead and Rajaratnam (1980) for uniformly rough boundaries. Preston tube measurements were made every 0.5 cm along the entire wetted perimeter of the flume at the same cross section, where the velocity measurements were made. To verify the streamwise uniformity of the flow field, a second set of Preston tube measurements, spaced 2 cm apart, was made at a cross section 1.55 m upstream.

Comparison to Measurements

Velocity

Measured and calculated streamwise velocity fields are shown in Figs. 4(a and b). Contours are drawn without smoothing using the computer software IDL. In general, the calculated velocity is in reasonable agreement with the magnitude and structure of the measured field. With respect to discharge, the calculated discharge ($0.405\ m^3/s$) is close to two independent measurements: (1) the discharge obtained from integrating the velocity measurements over the cross section ($0.373\ m^3/sec$, 8.6% difference) and (2) the discharge obtained from the flume's Venturi meter ($0.396\ m^3/sec$, 2.3% difference). Two possible reasons the predicted discharge is slightly higher than the measurements are that (1) there is more turbulent mixing in the flume than is present in the calculation and/or (2) the actual roughness (k_s) of the flume boundaries is greater than the roughness used in the calculation.

Additional turbulent mixing can be incorporated into the model by increasing the channel-scale eddy viscosity ($K_o=\kappa[g\sin(\theta)R]^{1/2}H/\beta$) through a change in β. Perfect agreement between the calculated discharge and the Venturi discharge measurement requires changing the value of β from 6.24 to 3, which more than doubles K_o. The relative insensitivity of the calculated discharge to substantial changes in K_o indicates that the magnitude of interior mixing is probably not the primary cause of the discharge discrepancy, and, for this reason, the original formulation for K_o will be retained.

Perfect agreement with the discharge also can be achieved by increasing the values of k_s used in the model by 50%. The original calculation employed standard values of k_s for the two distinct types of planar surfaces: aluminum and glued sand (see Table 1). Minor corrosion on the flume walls and irregularities in the sand surface could produce roughness heights 50% greater than was

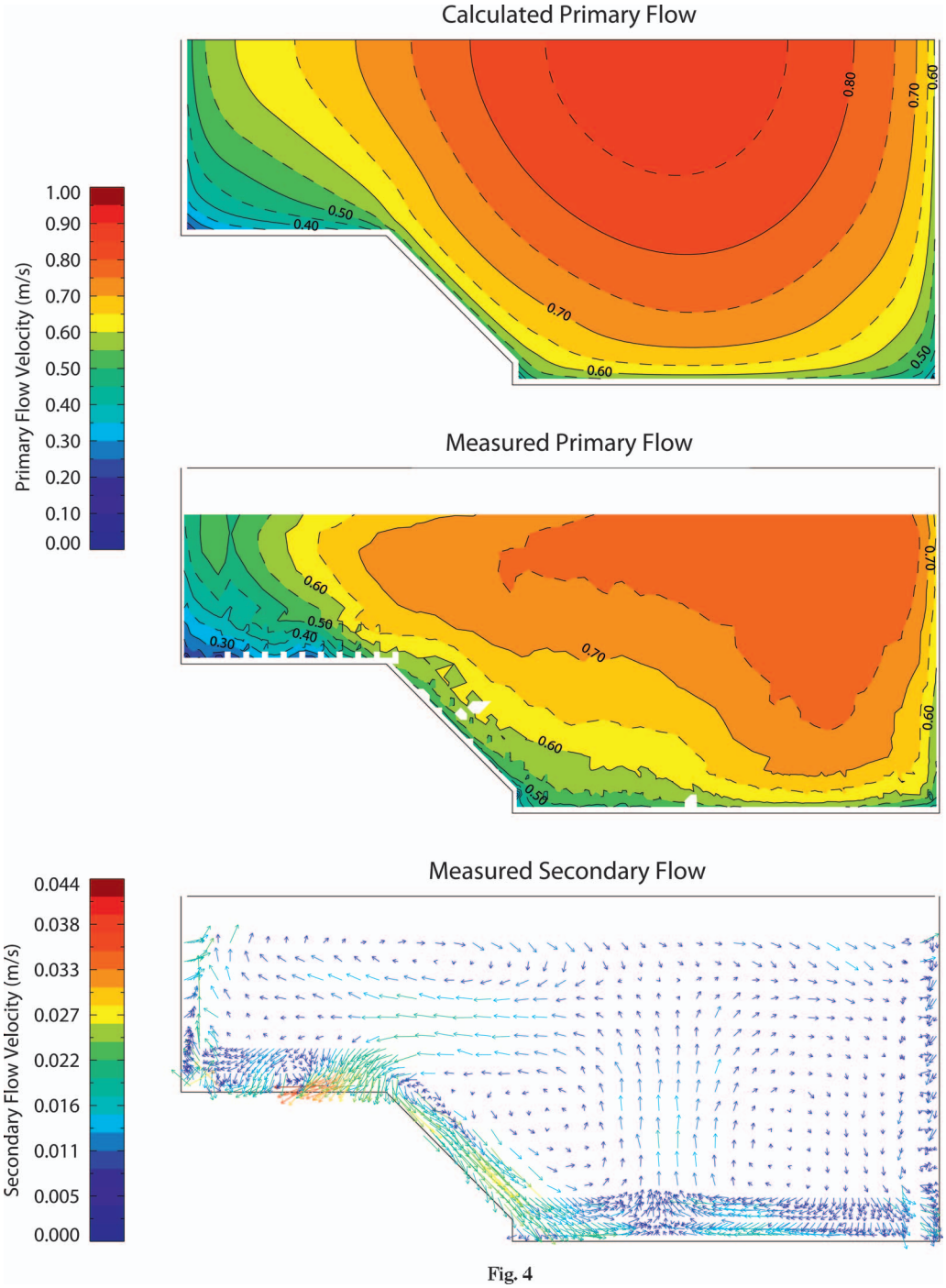

Fig. 4

Fig. 4. (Color) (a) Calculated downstream velocity; (b) measured downstream velocity; and (c) measured secondary circulation

assumed. Spatial variability in the roughness along the boundaries also would likely have an effect on the structure of the velocity field. Given the fairly good agreement between modeled and measured discharge based on the original values of k_s; however, no empirical adjustments in roughness will be made in remaining calculations of this paper. A test of validity of the roughness assumptions will be described in the next section.

In terms of the structure of the calculated and measured velocity fields, the agreement is best on the left side of the channel over the cobble-roughened "floodplain." The greatest difference in structure is associated with the shape and location of the high-velocity core (defined here to be the region of the velocity field, where $u > 0.7$ m/s). The outline of the calculated high-velocity core roughly follows the shape of the flume boundary, whereas the perimeter of the measured core is distorted away from the bed near the center of the flume and away from the flume walls near the surface. The complex shape of the measured high-velocity core is related to a well-developed secondary flow in the flume [Fig. 4(c)], which cannot be calculated from a ray-isovel model alone. Secondary flows similar to the one shown in Fig. 4(c) are common in straight flumes with prismatic cross-sections (e.g., Shiono and Knight 1991; Tominga and Nezu 1991). As mentioned earlier, many of these patterns are produced by geometric characteristics of laboratory flumes, such as sharp corners and

Table 2. Sum of Squared Error (SSE) for Calculated Velocity

	SSE/n (m^2/s^2)			
	Low velocity $u_{meas} < 0.5$ ($n=305$)	Medium velocity $0.5 < u_{meas} < 0.7$ ($n=872$)	High velocity $u_{meas} > 0.7$ ($n=324$)	All measurements ($n=1501$)
Calculated velocity (Fig. 3(b))	0.0053	0.0040	0.0041	0.0043
Perturb. of calculated velocity (Fig. 6)	0.012	0.0029	0.0033	0.0048

Note: SSE is normalized by the number of measurements (n) in each comparison.

long stretches of similar cross-sectional shape. Irregular natural channels contain different types of secondary circulations, which are generated from irregularities in the boundary and planform.

The secondary flow contains four main circulation cells: a pair of large oppositely rotating cells immediately above the bed and two smaller oppositely rotating cells located on either side of the channel just below the surface. The cross-stream and vertical flow in these cells redistributes the primary flow field by advecting low downstream momentum into areas of higher momentum and vice versa. The most noticeable example of this redistribution occurs just above the central portion of the flume bed. There, a well-defined stream of vertical flow transports near-bed low-momentum fluid up into the interior, which, in turn, alters the region of the high-velocity flow relative to what it would be if no secondary flow was present. A similar redistribution of momentum occurs near the surface, where low-momentum fluid near the top of both of the vertical flume walls is advected toward the center of the flume by the two near-surface circulation cells. This transport causes the maximum downstream velocity to occur below the surface and accounts for much of the difference between the measured and calculated velocity fields in the region beside the top of both flume walls. Further down the right wall, at about three-quarters of the flow depth, the measured high-velocity core is closer to right wall of the flume than was calculated by the model. This difference also is related to the secondary flow near the right wall of the flume, which is directed toward the right wall as seen in Fig. 4(c) and, thus, moves high momentum fluid from the interior closer to the wall.

A quantitative measure of the agreement between the measured and calculated velocity fields can be made by computing the sum of the squared error (SSE) of the calculation about the measurements. The sum of squared error is defined as $\Sigma_{i=1}^{i=n}[u_{meas\ i} - u_{calc\ i}]^2$, where u_{meas} is the measured velocity, u_{calc} is the calculated velocity, and n is the number of measurements. Table 2 contains a summary of the SSE normalized by n for all of the measurements, as well as for three velocity ranges: low, medium, and high. As seen in Table 2 there is not a substantial difference in the total error for the three velocity ranges. The average error in calculated velocity is 9.4% of the mean velocity.

Boundary Shear Stress

Measured and calculated boundary shear stress distributions are shown in Fig. 5. The similarity between the two measured boundary shear stress profiles made at $x=19.5$ m and $x=18.0$ m confirm that the streamwise flow field is nearly uniform. The variability in

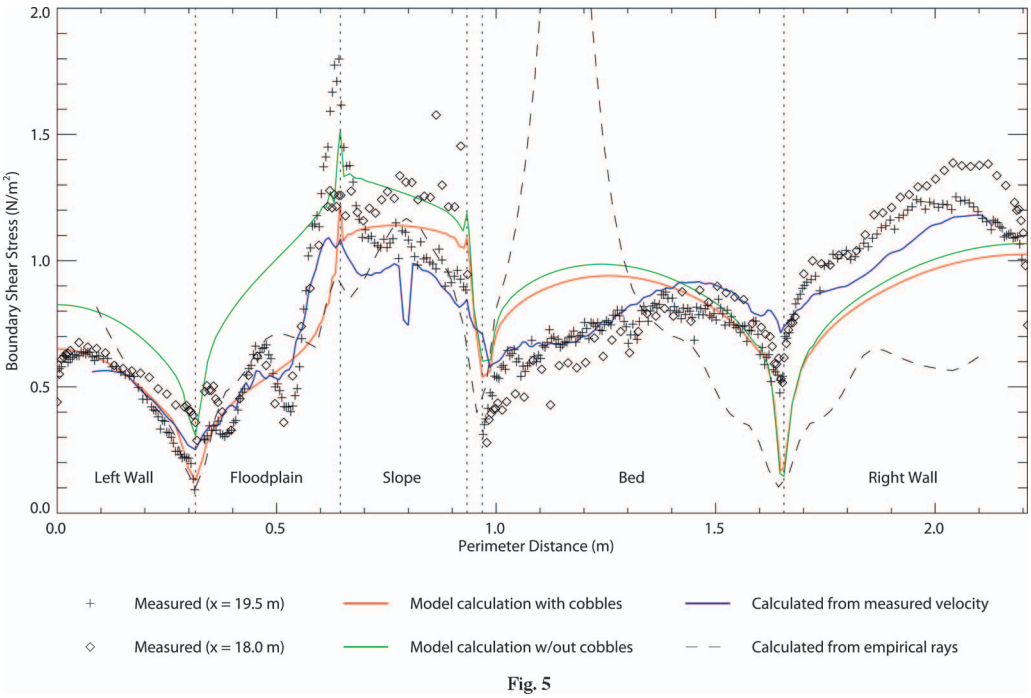

Fig. 5. (Color) Comparison of measured and calculated boundary shear stress distributions across the entire wetted perimeter. The measurements of boundary shear stress ("plus" and "diamond" symbols) were made with a Preston tube. The blue line is the stress distribution derived from the measured velocity field using Eq. (9). The vertical dotted lines denote the locations of the corners along the flume perimeter.

each measured stress profile demonstrates the importance of the high-resolution sampling. Had the measurements been made at a coarser resolution, it would have been impossible to distinguish the complex structure of the profile from measurement noise.

Despite the differences in calculated and measured velocity fields, the calculated boundary shear stress distribution (red line) does a reasonable job capturing the structure of the measured stress distributions. The model correctly predicts low-stress regions near the three sub-180° corners (base of left wall, base of slope, and base of right wall) and the high-stress area near the >180° corner between the floodplain and slope. On the floodplain, the primary reason the calculated stress profile differs in structure from the measured profile is due to the manner in which the drag on the cobbles is incorporated into the calculation. The ray-isovel model, which is designed for reach-averaged cross sections of natural channels, does not model the flow around individual cobbles. Rather, the model determines the reach-averaged velocity field in the cobble zone based on the assumption that the cobbles are randomly distributed throughout the floodplain. In contrast, the measured stress profiles on the floodplain, which were made at cross sections where the Preston tube could be positioned between the staggered cross-stream rows of cobbles, depend on the location of the Preston tube relative to nearby cobbles. The two measured low-stress regions along the floodplain correspond to measurement positions just downstream from a cobble.

For reference, the calculated boundary shear stress distribution without cobbles is shown with the green line in Fig. 5. Comparison of this distribution with the measurements and calculation with cobbles (red line) shows that the drag on the cobbles has a substantial effect on the boundary shear stress on the left half of the flume. The form drag on the cobbles reduces the stress that is transmitted directly to the left wall and floodplain surface of the flume.

The greatest differences between the measured boundary shear stress distribution and the calculation with cobbles are along the bed and right wall of the flume. These differences are related to the relative locations of the high-velocity core, which, in turn, are related to the presence of secondary flow in the flume and the absence of secondary flow in the calculation. On the bed, the location of maximum boundary shear stress in both the measurements and the calculation corresponds to the lateral position of the maximum velocity. The calculated position of maximum velocity is slightly left of the center of the bed, but the measured position is close to the right wall, as a result of the circulation field over the bed. Secondary flow patterns in the flume also have pushed the high-velocity core closer to the right wall, resulting in high wall stress. The calculated stress on the wall, which is ~20% lower than the measured stress, is similar in magnitude to the calculated bed stress. This similarity is due to the facts that (1) the calculation contains no secondary circulations that would redistribute downstream momentum; and (2) the roughness of the bed and the wall area are assumed to be equal.

The boundary shear stress distribution also can be derived from the measured velocity field. One way to do this is to compute stress from the velocity field using the law of the wall. This is done here to evaluate the roughness assumptions used in the calculation and further investigate the connection between the measured boundary shear stress distribution and the structure of the velocity field. Velocity-derived estimates of boundary shear stress at any point along the wetted perimeter can be determined by

$$\tau_b = \rho\left(\frac{u_{\text{meas}}\kappa}{\ln(l_{\text{meas}}/l_o)}\right)^2 \tag{9}$$

In Eq. (9), u_{meas} is the velocity a short distance, l_{meas}, from the boundary, and l_o is the local roughness height of the boundary. The variable l_{meas} could be defined simply as a fixed perpendicular distance away from the boundary. Alternatively, l_{meas} could be defined using curvilinear rays, which provide a better representation of the stress in the corners. The latter approach is taken here using the calculated ray field. Specifically, l_{meas} is defined to be 8% of the total length of a ray at the position for which the boundary shear stress is being determined. This distance is sufficiently close to the wall that the velocity profile along the rays is nearly logarithmic.

The boundary shear stress distribution determined using Eq. (9) is shown with the blue line in Fig. 5. The close agreement between this distribution and the measurements reinforces several important conclusions regarding the experiment. First, it demonstrates that the independently measured velocity and boundary shear stress fields are consistent with each other and that they are measured accurately. Second, the agreement provides additional evidence that the measured stress distribution is related to the position of the high-velocity core. And lastly, the agreement shows that the standard values of k_s used to represent the roughness of the flume boundaries are reasonable and that the major differences between the calculations and the measurements can be attributed to the secondary flow.

Another way to compute boundary shear stress from the measured velocity field is to apply the ray-isovel approach empirically in the manner of Leighly (1932). This is done by first computing the rays for a measured velocity and then applying Eq. (2) to compute the stress based on area between the rays. Smoothing is applied to the measured velocity field in order to reduce variability in the computed boundary shear stress distribution. The boundary shear stress computed using this method is shown with the dashed line in Fig. 5. Over much of the wetted perimeter, the boundary shear stress distribution computed using the empirical rays (dashed line) is in poor agreement with the measurements. The biggest discrepancy occurs over the bed where the empirical application of the ray-isovel approach incorrectly predicts a large spike in the bed stress. This spike is caused by the low-velocity zone in the measurements above the left-center portion of the bed, which distorts the rays to produce the high-stress zone on the bed. The major discrepancy in boundary shear stress illustrates one of the problems in calculating boundary shear stress distributions from rays obtained from measured velocity fields containing significant secondary circulations: small distortions in a measured velocity field can result in large distortions to the calculated stress distribution. A second albeit smaller problem associated with deriving boundary shear stress distributions using empirical rays occurs when the highest velocity is below the free surface, as is the case in the study flume. In this situation, strict application of the ray-isovel approach assigns a portion of the boundary stress to the free surface rather than to the solid boundary. Although, the empirical application of the ray-isovel approach performs poorly in the flume situation, it should be reiterated that the approach, as applied theoretically in the flow model described above, provides a reasonably accurate representation of the boundary shear stress field.

As with the velocity field, a quantitative measure of the agreement between the measured and calculated boundary shear stress distributions can be made by computing the sum of the squared error between measurements and the calculation. The normalized

Table 3. Sum of Squared Error (SSE) for the Calculated Boundary Shear Stress Distributions Shown in Figs. 4 and 6

	SSE/n (N^2/m^4)					
	Left wall	Floodplain	Slope	Bed	Right wall	All meas.
Model with cobbles (red line, Fig. 5)	0.006 (76)	0.073 (90)	0.026 (63)	0.037 (185)	0.073 (103)	0.044 (518)
Model w/out cobbles (green line, Fig. 5)	0.042 (76)	0.14 (90)	0.035 (63)	0.052 (185)	0.062 (103)	0.065 (518)
From meas. Velocity (blue line, Fig. 5)	0.005 (51)	0.038 (90)	0.068 (63)	0.014 (185)	0.014 (81)	0.025 (471)
From empirical rays (dashed line, Fig. 5)	0.012 (49)	0.092 (90)	0.062 (63)	0.75 (185)	0.35 (78)	0.38 (466)
Perturb. of calculated velocity (Fig. 6)	0.011 (76)	0.072 (90)	0.019 (63)	0.028 (185)	0.034 (103)	0.033 (518)

Note: SSE is normalized by the number of measurements in each comparison, which is listed in parentheses.

sum of squared error for each of the four boundary shear stress calculation methods shown in Fig. 5 is given in Table 3, which lists the normalized sum of squared error for each segment of the wetted perimeter, as well as for the entire wetted perimeter.

Perturbation of Calculated Velocity Field

It is likely that better agreement with the measurements could be achieved using a fully three-dimensional model capable of resolving the complex secondary flow field. Before adopting a more complicated model, it is important to evaluate whether or not the simple ray-isovel scheme produces a zero-order solution, which can, if necessary, be perturbed with a known or estimated secondary flow to produce realistic first-order streamwise velocity fields (i.e., a streamwise velocity field that includes the effects of the secondary flow). A very simple test of this is done here by perturbing the calculated velocity field with the measured secondary circulation. The perturbation assumes that (1) the secondary flow patterns shown in Fig. 4(c) developed uniformly across the cross section, (2) the circulation developed linearly after half the distance from the entrance to the measurement section, and (3) the travel time to the measurement section is suitably approximated by the average streamwise velocity at the section divided by the travel distance (t=27 sec). Using these assumptions, a distortion length and direction can be defined for every point where the secondary flow is known. A small amount of smoothing is applied to the measured secondary flow to reduce small-scale variability in the measurements. The perturbed velocity field is created by resampling the calculated velocity field at locations defined by the distortion vectors. To illustrate the perturbation procedure, a sample calculation of the distortion vector ($\vec{l}_{\text{distort}}$) at one point in the flume (0.085 m above the bed and 0.45 m away from the right wall) is described. At this point the calculated primary flow is 0.72 m/s, and the measured secondary flow velocity has a vertical component w=0.012 m/s and a negligible cross-stream component. On the basis of the assumed rate of development for the circulation, $\vec{l}_{\text{distort}}$ corresponds to $-w\,t/4$, or −0.082 m in the vertical direction. Resampling the calculated primary flow field at a position $\vec{l}_{\text{distort}}$ away from the starting point gives a lower velocity of 0.60 m/s. This calculation represents lower momentum fluid near the boundary being transported upward to the interior by the vertical secondary flow. Repeating the above calculation throughout the entire cross section yields the distorted field shown in Fig. 6(a). Although the above algorithm does not employ the continuity equation to impose a consistency on the secondary flow field, it does provide a simple way to evaluate whether or not the ray-isovel model produces an acceptable zero-order flow field for use in a perturbation analysis.

Although the distorted field shown in Fig. 6(a) is not in perfect agreement with the measured field [Fig. 4(b)], it exhibits several features in common with the measurements that were not present in the original calculation. Above the bed, the high-velocity core of the distorted velocity field is pushed away from the boundary like that of the measurements. The core of the distorted field also is in better agreement with the measurements near the top of the right wall, as a result of being pushed closer to the right wall by the secondary flow. Lastly, the distortion has shifted the elevations of maximum velocity across the flume from the surface to approximately the same elevation as the maximum velocities in the measurements ($z \approx 3/4H$). The discrepancies between distorted and measured fields could be related to the manner in which the secondary flow field evolved from the entrance of the flume to the measurement section. No ADV velocity data are available upstream of the measurement section to document that evolution, and, in lieu of such data, the perturbation analysis made the simple assumption that the centroids of the measured circulation cells were stationary and that all circulation cells developed at the same rate. It is likely that the circulation developed differently from what was assumed. For example, secondary flow probably would have developed first in the lower right corner of the flume such that it occupied most of the lower portion of the channel, because the gradients in the turbulent properties for this situation are greatest. The circulation cell in the lower left part of the flume adjacent to the slope probably developed later. Perturbation of the calculated field using this more complex evolution of the secondary flow may produce better agreement with the measured field; however, such an evolution is difficult to reconstruct and impossible to verify without three-dimensional velocity information from upstream.

Quantitative measures of the agreement between the distorted velocity field and the measurements are given in Table 2 (summary of sum of squared error) and Fig. 6(b) (plot of error). Although the sum of squared error in the low-velocity range is greater than the original calculation, the error is considerably less over the medium- and high-velocity ranges, which occupy over 90% of the measurement domain. Additional information regarding the distribution of error across the cross section for the distorted and original undistorted cases is shown in Figs. 6(b and c), respectively. Both the error statistics listed in Table 2 and the difference plots shown in Figs. 6(b and c) show that the perturbed

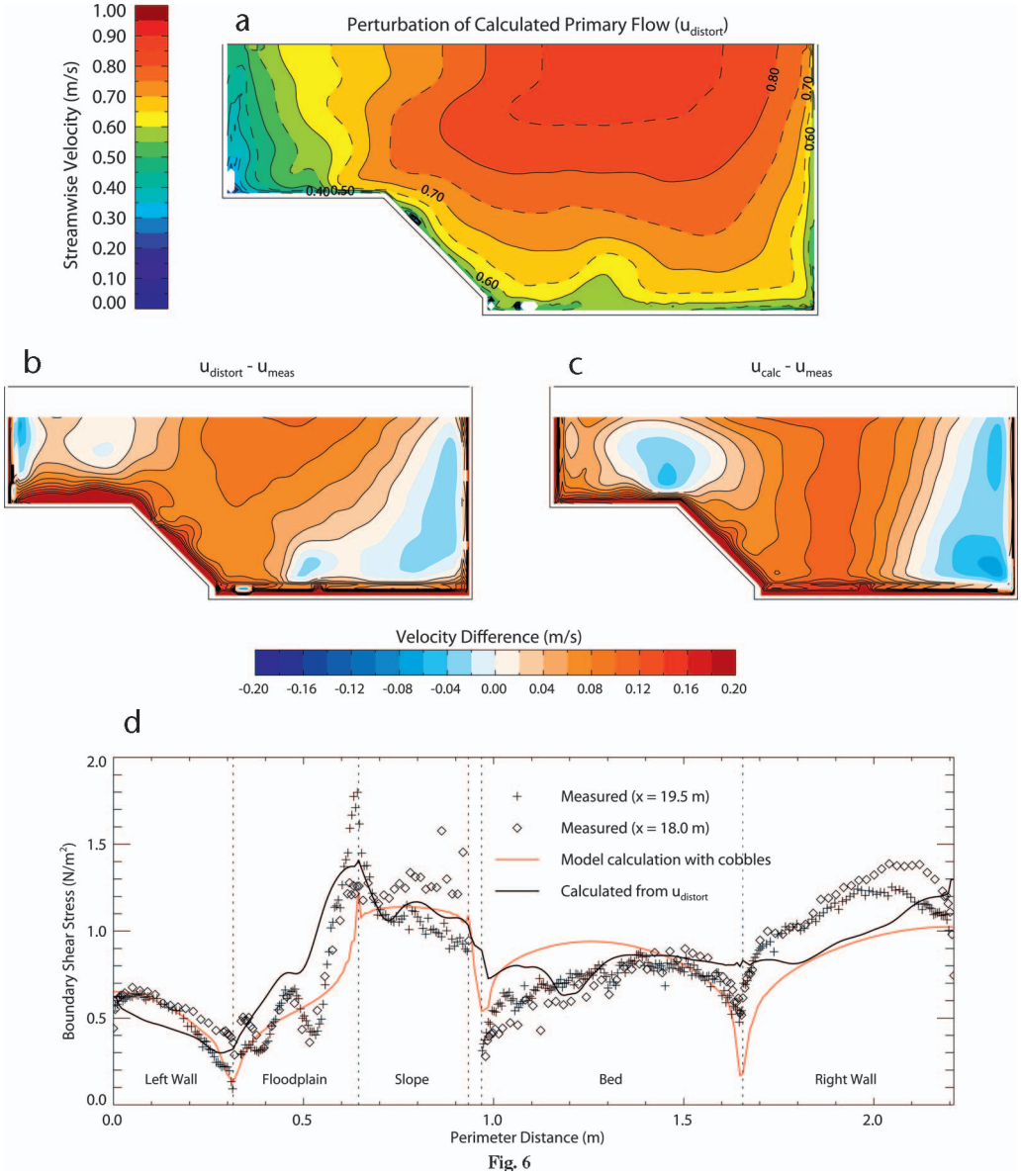

Fig. 6

Fig. 6. (Color) (a) Perturbation of calculated primary flow with measured secondary circulations ($u_{distort}$); (b) difference between $u_{distort}$ and measured velocity [u_{meas}, Fig. 4(b)]; (c) difference between original calculation [u_{calc}, Fig. 4(a)] and u_{meas}; and (d) calculated boundary shear stress distribution based on distorted velocity field. The measurements and the original stress calculation (from Fig. 5) are replotted for comparison.

velocity field is in better agreement with the measurements than the original calculation over most of the measurement domain.

The law of the wall can be used to calculate the boundary shear stress distribution for the perturbation of the calculated primary flow. The stress distribution computed with Eq. (9) using the distorted velocity field in place of u_{meas} is shown in Fig. 6(d). For comparison, the calculated stress from the original model (Fig. 5, red line) also is shown. although the calculated stress based on the distorted flow is not in perfect agreement with the measurements of stress, it is in slightly better agreement than the measurements than the original calculation, particularly over the bed and wall. The sum of squared error for the calculated stress distribution is listed in Table 3.

The improved agreement between the measured and distorted flow and boundary shear stress fields suggest that the ray-isovel model provides (1) a reasonable estimate of the flow field when systematic secondary circulations are absent and (2) a zero-order flow field that is suitable for perturbations using known or calculated secondary flows. Both of these features are important for application to natural channels. Natural channels typically contain a variety of boundary and planform irregularities, which produce small-scale secondary flow patterns that are different from the systematic circulation observed in the flume. The model is well suited for computing reach averaged velocity and boundary shear stress fields in these types of channels, because reach averaging tends to remove the effects of the local secondary flow patterns generated by the boundary irregularities.

Variation of Boundary Shear Stress with Width-to-Depth Ratio

Provided the level of agreement between the modeled and measured boundary shear stress is considered acceptable, the model

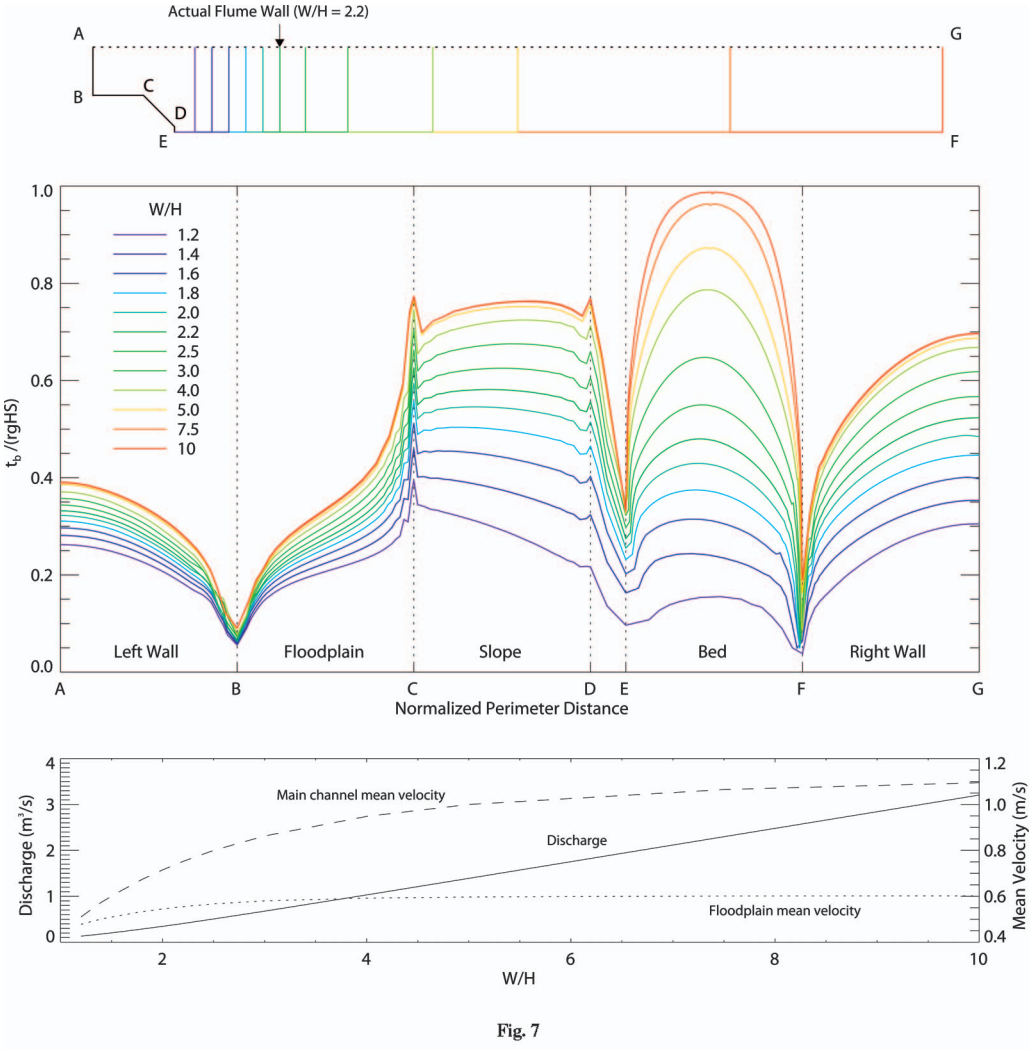

Fig. 7

Fig. 7. (Color) (a) Calculated boundary shear stress and (b) mean flow velocity and discharge for flume channels with varying right wall locations. The channel geometry for each case is shown with no vertical exaggeration at the top of the figure. The actual flume geometry corresponds to the case $W/H=2.2$. The boundary shear stress is normalized by the depth-slope product, which is 1.96 $\mathrm{N/m^2}$.

can be used to generalize the experimental results to both wider and narrower flume geometries. In this section, model results from two different variations of the original flume configuration are presented. The first scenario, shown in Fig. 7, depicts the variation in boundary shear stress profiles for 12 different positions of the right wall of the flume. In each of these cases, the depth, slope, roughness, and left bank geometry remains identical to the original flume geometry. The second scenario, shown in Fig. 8, presents a similar set of 10 cases in which the position of only the left wall of the flume is changed. These latter cases have floodplains of varying widths, which are roughened by cobbles having the same mean diameter and spacing as was present in the original flume. The calculated discharge for all of the cases varies as function of width and is shown in Figs. 7(b) and 8(b). Figures 7(b) and 8(b) also contain the mean velocity and area for the floodplain and main channel. The floodplain and main channel portions of the channel are defined to be the respective sections to the left and right of corner "C" in Figs. 7 and 8. Calculated Reynolds numbers indicate the flow is turbulent for all cases.

To facilitate comparisons between the boundary shear stress profiles of the cases in Figs. 7(a) and 8(a), the perimeter distance (x-axis) has been normalized by the length of each segment of the boundary. Note in Fig. 7 that the walls, floodplain, and slope have the same dimensions; only the bed segment of the wetted-perimeter changes length with each case. Similarly, in Fig. 8, the floodplain segment is the only portion of the wetted perimeter that changes dimension with each case. Also, note in Fig. 7 that as the flume widens (and the hydraulic radius increases), there is a corresponding increase in the average boundary shear stress due to the integral constraint that the average boundary shear stress plus the drag stress on the cobbles equals $\rho g \sin(\theta) R$. Similar changes in the average stress are not immediately apparent in Fig. 8, because the geometric variations of that scenario result in only minor changes in the hydraulic radius with each case.

There are several common characteristics to the calculations presented in Figs. 7 and 8. In both geometric scenarios, the boundary shear stress in the central portion of the width-varying segment (bed segment in Fig. 7, floodplain segment in Fig. 8) does not reach its asymptotic limit until the width-to-local-depth ratio is $\sim$10. For the scenario shown in Fig. 7, this limit corresponds to the depth-slope product, $\rho g \sin(\theta) H$. For the changing floodplain scenario (Fig. 8), the asymptotic limit of boundary shear stress on the cobble roughened floodplain is the floodplain depth-slope product minus the drag stress on the cobbles. In the

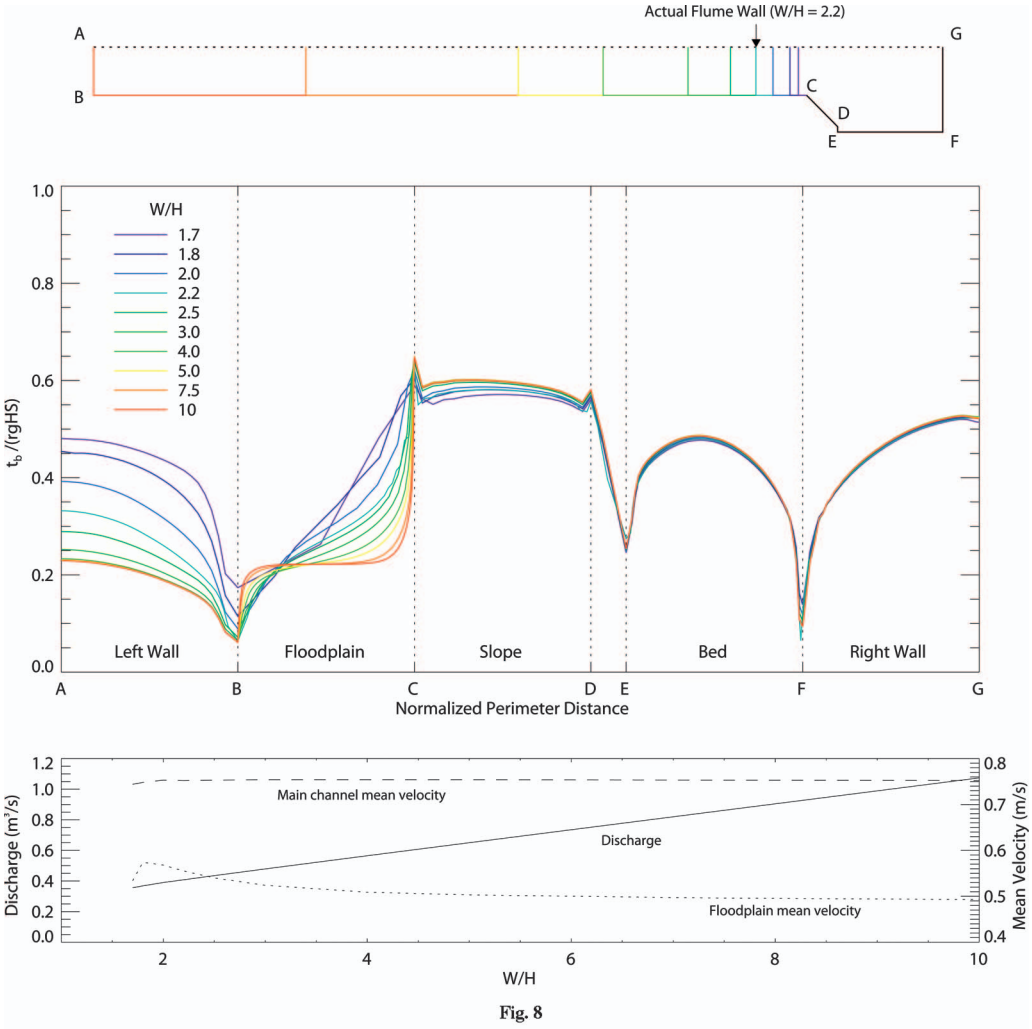

Fig. 8

Fig. 8. (Color) (a) Calculated boundary shear stress; (b) mean flow velocity and discharge for flume channels with varying left wall locations. The boundary shear stress is normalized in the same manner as was done in Fig. 7. For reference, the floodplain depth-slope product is 57% of $\rho g \sin(\theta) H$. The asymptotic limit of stress on the floodplain is ~39% of the floodplain depth-slope product due to the drag on the floodplain cobbles. Note that varying the width of the floodplain has essentially no effect on the stress on the bed and the right wall of the channel.

widest cases in Fig. 8, the drag stress is 39% of the floodplain depth-slope product. A second feature common to both geometric scenarios shown in Figs. 7 and 8 is that the stress in the three sub-180° corners (B, E, and F) is very insensitive to the width-to-depth ratio. This is because corner stresses are primarily controlled by the geometry (specifically, the radius of curvature) of the corner. Rounder flume corners would have produced more gradual transitions in the stress between the linear segments of the flume boundary. Another interesting feature shared by the two sets of calculations, is that the stress on the opposite side of the channel from the moveable wall is relatively insensitive to the width-to-depth ratio. This feature is strongly present in the set of calculations shown in Fig. 8(a) and weakly present in the scenario shown in Fig. 7(a). The main reason the stress on the left side of the channels in Fig. 7(a) is less sensitive to changes in the width-to-depth ratio than the stress on the right side of the channels is because the high roughness of the cobble-roughened floodplain dominates the near-bank flow and boundary shear stress fields. In Fig. 8(a), the boundary shear stress on the bed and right walls is insensitive to changes in floodplain width, because the flow in the main channel is controlled primarily by the flow depth and geometry of the right side of the channel. Figs. 7(b) and 8(b) show similar trends for the mean velocity of the two "halves" of the channel. The mean velocity in the "half" of the channel that does not vary in width quickly reaches a constant value.

Summary and Conclusions

A comprehensive data set of velocity and boundary shear stress measurements made in a laboratory flume with a complex cross section is presented. These measurements were used to test the relatively simple model of Kean and Smith (2004) for determining the vertical and lateral distributions of streamwise velocity and boundary shear stress in a channel. The high resolution of the measurements makes this data set suitable for testing other flow models, such as more complicated fully three-dimensional flow models, which are not addressed here. The simple model tested in this paper accommodates lateral boundaries and is extended here to also determine the flow effects of drag on clasts in the study channel. The model was applied in a fully predictive mode (i.e.,

no parameters were adjusted empirically to achieve better agreement with the data). Differences between the modeled and measured velocity and boundary shear stress distributions are primarily due to secondary circulations in the flume, which are not included in the model. In spite of this simplification, the modeled velocity and boundary shear stress distributions were shown to reproduce adequately the essential patterns of the measured fields, as well as the discharge. The agreement with discharge reinforces the utility of the approach for calculating theoretical stage-discharge relations in narrow channels (see Kean and Smith 2005), which requires careful determination of the contributions to flow resistance from the bed, walls, and large roughness elements in the channel.

Better agreement with the structure of the measured velocity and stress fields was achieved by distorting the calculated field using the measured secondary flow. This agreement demonstrates that the ray-isovel model yields zero-order flow fields suitable for perturbation analysis. This second step, which is not taken here but is described in Kean (2003), is necessary for accurately resolving the near-bank velocity and boundary shear stress distribution in curved channels. Including the effects of secondary circulations, however, is not required to adequately compute the reach-averaged velocity and boundary shear stress distributions in relatively straight natural channels (e.g., Griffin et al. 2005), because reach-averaging tends to remove the effects of the local secondary flow patterns generated by the boundary irregularities.

After demonstrating that the model adequately reproduces the measured velocity and shear stress distributions, the model was then used to investigate the variability in the profiles of boundary shear stress to changes in the width-to-depth ratio of a hypothetical channel having similar characteristics to the study channel. These simulations demonstrated that the flow resistance of the banks had a substantial effect on the bed boundary shear stress, even for wide cases.

The aspects of this study that are unique include the commensurate high-resolution velocity field, high resolution of the boundary shear stress cross-stream profiles, test of the assumption of two-dimensional flow using paired boundary shear stress profiles, and a predictive calculation that resolves the lateral shear stress field. By combining procedures to quantify the roughness of the bed and the banks with a model such as the one described in this paper, it is possible to determine accurately the near-bank velocity and boundary shear stress field in natural channels. This ability, when combined with sediment transport algorithms, provides a foundation for determining rates and patterns of geomorphic adjustment in streams, rivers, rills, and gullies.

Acknowledgments

John Cox made most of the detailed flume measurements that were used in this study. Robert Wells provided additional measurement support. Ned Andrews, Jeff Coe, and three anonymous reviewers made many helpful suggestions.

Notation

The following symbols are used in this paper:

A = total cross-sectional area of channel;
C_D = drag coefficient;
D = mean diameter of cobbles;
d = mean width of the cobbles at an elevation z;
F = drag force per unit volume;
$\bar{F}(l)$ = average of F along length of isovel between two rays;
g = acceleration of gravity;
H = maximum flow depth;
K = scalar eddy viscosity;
K_o = channel scale eddy viscosity;
k_s = equivalent grain size of surface;
L = length of the ray from the boundary to the surface;
l = distance along a ray from the boundary;
l_d = dummy integration variable along ray;
l_o = boundary roughness height;
$\vec{l}_{\text{distort}}$ = distortion vector;
P = full wetted perimeter;
p_b = perimeter length along the boundary between two rays;
$p(l)$ = length along the isovel between two rays;
R = hydraulic radius;
u = downstream velocity;
u_{ref} = reference velocity;
u_* = shear velocity;
v = cross-stream velocity;
W = width of channel;
w = vertical velocity;
x = downstream direction;
y = cross-stream direction;
z = vertical direction;
β = constant;
θ = angle deviation of the water surface from horizontal;
κ = von Karman's constant;
λ = mean spacing of the cobbles;
ρ = density of water;
τ_b = local boundary shear stress;
τ_{lx} = shear stress along each ray in the interior of the channel;
τ_{yx} = yx components of the deviatoric stress tensor;
τ_{zx} = zx components of the deviatoric stress tensor; and
$\bar{\tau}_b$ = average boundary shear stress.

References

Cheng, N. S., and Chua, L. H. C. (2005). "Comparisons of sidewall correction of bed shear stress in open-channel flows." *J. Hydraul. Eng.*, 131(7), 605–609.

Einstein, H. A. (1942). "Formulas for the transportation of bed load." *Trans. Am. Soc. Civ. Eng.*, 107, 561–577.

Einstein, H. A. and Chien, N. (1955). "Effects of heavy sediment concentrations near the bed on velocity and sediment distribution." Univ. of California, Berkeley, Institute for Engineering Research, No. 8.

Griffin, E. R., Kean, J. W., Vincent, K. R., Smith, J. D., and Friedman, J. M. (2005). "Modeling effects of bank friction and woody bank vegetation on channel flow and boundary shear stress in the Rio Puerco, New Mexico." *J. Geophys. Res.*, 110, F04023.

Head, M. R., and Rechenberg, I. (1972). "The Preston tube as a means of measuring skin friction." *J. Fluid Mech.*, 14, 1–17.

Hollingshead, A. B., and Rajaratnam, N. (1980). "A calibration chart for the Preston tube." *J. Fluid Mech.*, 14, 1–17.

Houjou, K., Shimizu, Y., and Ishii, C. (1990). "Calculation of boundary shear stress in open channel flow." *J. Hydrosci. Hydr. Eng.*, 8, 21–37.

Hwang, L.-S., and Laursen, E. (1963). "Shear measurement technique for

rough surfaces." *J. Hydr. Div.*, 89(HY2), 19–37.
Kean, J. W. (2003). "Computation of flow and boundary shear stress near the banks of streams and rivers." Ph.D. thesis, University of Colorado, Boulder.
Kean, J. W., and Smith, J. D. (2004). "Flow and boundary shear stress in channels with woody bank vegetation." *Riparian vegetation and fluvial geomorphology*, AGU Water Science and Application Series 8, S. J. Bennett and A. Simon, eds., AGU, Washington, D.C., 237–252.
Kean, J. W., and Smith, J. D. (2005). "Generation and verification of theoretical rating curves in the Whitewater River Basin, KS." *J. Geophys. Res.*, 110, F04012.
Kean, J. W., and Smith, J. D. (2006a). "Form drag in rivers due to small-scale natural topographic features: 1. Regular sequences." *J. Geophys. Res.*, 111, F04009.
Kean, J. W., and Smith, J. D. (2006b). "Form drag in rivers due to small-scale natural topographic features: 2. Irregular sequences." *J. Geophys. Res.*, 111, F04010.
Knight, D. W., Demetriou, J. D., Hamed, M. E. (1984). "Boundary shear in smooth rectangular channels." *J. Hydraul. Eng.*, 110(4), 405–422.
Knight, D. W., Yuen, K. W. H., and Al-Hamid, A. A. I. (1994). "Boundary shear stress distributions in open channel flow." *Mixing and transport in the environment*, K. J. Beven, P. C. Chatwin, and J. H. Millbank, eds., Wiley, Hoboken, N.J., 51–87.
Kundu, P. K. (1990). *Fluid mechanics*, Academic, New York.
Leighly, J. B. (1932). "Toward a theory of the morphologic significance of turbulence in the flow of water in streams." *Univ. Calif. Publ. Geogr.*, 6(1), 1–22.
Liggett, J. A. (1994). *Fluid mechanics*, McGraw-Hill, New York.
Long, C. E., Wiberg, P. L., and Nowell, A. R. M. (1993). "Evaluation of von Karman's constant from integral flow parameters." *J. Hydraul. Eng.*, 119, 1182–1190.
Lundgren, H., and Jonsson, I. G. (1964). "Shear and velocity distribution in shallow channels." *J. Hydr. Div.*, 90(HY1), 1–21.
Maghrebi, M. F., and Ball, J. E. (2006). "New method for estimation of discharge." *J. Hydraul. Eng.*, 132, 1044–1051.
Naot, D., Nezu, I., and Nakagawa, H. (1993). "Hydrodynamic behavior of compound rectangular open channels." *J. Hydraul. Eng.*, 119, 390–408.
Nece, R. E., and Smith, J. D. (1970). "Boundary shear stress in rivers and estuaries." *J. Wtrwy., Harb. and Coast. Engrg. Div.*, 96(WW2), 335–358.
Nezu, I., and Nakagawa, H. (1993). *Turbulence in open-channel flows*, Balkema, Rotterdam, The Netherlands.
Nikuradse, J. (1933). "Stromungsgesetze in rauhen Rohren." *VDI-Forschungsheft 361* (English translation, 1950, "Laws of flow in rough pipes." *NACA Tech. Mem. 1292*, Natl. Advis. Comm. for Aeron., Washington D.C.).
Parker, G. (1978). "Self-formed straight rivers with equilibrium banks and mobile bed. Part 2. The gravel river." *J. Fluid Mech.*, 89, 127–146.
Patel, V. C. (1965). "Calibration of the Preston tube and limitations on its use in pressure gradients." *J. Fluid Mech.*, 23(1), 185–208.
Preston, J. H. (1954). "The determination of turbulent skin friction by means of Pitot tubes." *J. R. Aeronaut. Soc.*, 58, 109–121.
Shimizu, Y. (1989). "Effects of lateral stress in open channel flow." *Rep. to the River Hydraulics and Hydrology Laboratory*, Civil Engineering Research Institute, Hokaido, Japan.
Shiono, K., and Knight, D. W. (1991). "Turbulent open-channel flows with variable depth across the channel." *J. Fluid Mech.*, 222, 617–646.
Tominaga, A., and Nezu, I. (1991). "Turbulent structure in compound open-channel flows." *J. Hydraul. Eng.*, 117(1), 21–41.
Vanoni, V. A., and Brooks, N. H. (1957). *Laboratory studies of the roughness of and suspended load of alluvial streams*, Sedimentation Laboratory, California Institute of Technology, Pasadena, Calif.
Wahl, T. L. (2000). "Analyzing ADV data using WinADV." *Proc. Joint Conf. on Water Resources Engineering and Water Resources Planning & Management*, ASCE, Reston, Minneapolis.
Wiberg, P. L., and Smith, J. D. (1991). "Velocity distribution and bed roughness in high-gradient streams." *Water Resour. Res.*, 27(5), 825–838.
Williams, G. P. (1970). "Flume width and water depth effects in sediment transport experiments." *U.S. Geological Survey Professional Paper, 562-H*.
Wu, S., and Rajaratnam, N. (2000). "A simple method for measuring shear stress on rough boundaries." *J. Hydraul. Res.*, 38(5), 399–400.
Yang, S. Q. and Lim, S. Y. (2005). "Boundary shear stress distributions in trapezoidal channels." *J. Hydraul. Res.*, 43(1), 98–102.